Nanoscale Advances

ROYAL SOCIETY OF CHEMISTRY

PAPER

View Article Online
View Journal | View Issue

Cite this: *Nanoscale Adv.*, 2025, **7**, 2585

A comparative study on the synthesis strategies and electrochemical features of bimetallic Cu/Co-MOFs†

Mohan Rao Tamtam,[a] Rui Wang,[b] Ravindranadh Koutavarapu,[c] Gyu Sang Choi,*[a] Jaesool Shim,*[b] Nguyen To Hoai*[de] and Nam Nguyen Dang [de]

Received 4th January 2025
Accepted 24th February 2025

DOI: 10.1039/d5na00019j

rsc.li/nanoscale-advances

In this work, three distinct synthetic procedures—step-by-step (CC-1), single-step (CC-2), and simple mixing (CC-3)—were utilized to investigate their effects on the formation of heterostructures in bimetallic Cu/Co-MOFs. The resulting MOF crystal structures revealed a 1 : 1 ratio of Co to Cu metal ions, and compared their electrochemical activities with a simple mixture of individual MOFs. To maximize the benefits of these synthesis approaches for supercapacitor uses, electrochemical analyses were conducted. Results revealed that the capacitance of CC-1 was 438 F g^{-1} at 1 A g^{-1}, which was 1.14 times and 2.76 times higher than those of the CC-2 and CC-3 samples, respectively. This notable performance was attributed to the synergistic contributions from each 2D material component and the formation of a stable heterostructure that resulted from an optimal metal-ion loading. The best-performing CC-1 electrode was further tested in both asymmetric (AD) and symmetric (SD) coin cell devices. AD demonstrated an energy density (ED) of 40.4 W h kg^{-1} through a power density (PD) of 302.3 W kg^{-1} with 75% stability, while the SD device displayed an ED of 15.7 W h kg^{-1} and a PD of 346.7 W kg^{-1} with 88% stability.

1. Introduction

The urgent need to improve energy storage systems and technologies is driven by growing environmental concerns. Additionally, there is an escalating demand for advanced power solutions in smart grids and electric vehicles. Supercapacitors (SCs), as a new type of large-capacity energy storage device, have demonstrated significant potential in this regard owing to their impressive power density and exceptional cycle life.[1] These attributes make them particularly well-suited to meet the energy storage needs of industrial equipment, transportation, and electronic devices. However, their relatively low ED poses a challenge for high-energy and high-power applications. Electrostatic mechanisms facilitate charge storage in conventional electrical double-layer capacitors (EDLCs) *via* rapid ion adsorption onto the electrode surfaces.[2] However, this ion adsorption process imposes a fundamental constraint on the achievable capacitance, primarily owing to the inherent limitations associated with the electrochemical double layer formation and the finite ionic mobility at the electrode/electrolyte interface. Conversely, pseudocapacitive (PC) materials, including transition metal compounds, activated carbons, MOFs, and conductive polymers, provide high specific capacitance by storing electrical energy through redox reactions.[2–7] However, they face significant limitations in cycle stability. Hybrid supercapacitors (HSs), which integrate EDLC-type anodes with battery-type cathodes, have shown notable benefits in terms of their operating voltage range and ED.[6] To further advance the development of HSs, the creation of new high-performance electrode materials is essential. Recently, hybrid supercapacitors have attracted significant interest as a viable alternative to EDLCs or PCs.[8] Hybrid SCs can function across a wider voltage range and offer higher capacitance owing to their combination of a carbon-based capacitive electrode with a battery-like electrode made from transition metals. These improvements address some of the limitations of conventional EDLCs and make hybrid supercapacitors a compelling option for advanced energy storage solutions.

[a]*School of Computer Science and Engineering, College of Digital Convergence, Yeungnam University, Gyeongsan 38541, Republic of Korea. E-mail: castchoi@ynu.ac.kr*

[b]*School of Mechanical Engineering, College of Engineering, Yeungnam University, Gyeongsan 38541, Republic of Korea. E-mail: jshim@ynu.ac.kr*

[c]*Physics Division, Department of Basic Sciences and Humanities, GMR Institute of Technology, Rajam 532 127, Andhra Pradesh, India*

[d]*Future Materials & Devices Lab., Institute of Fundamental and Applied Sciences, Duy Tan University, Ho Chi Minh City, 70000, Vietnam. E-mail: nguyentohoai@duytan.edu.vn*

[e]*The Faculty of Environmental and Chemical Engineering, Duy Tan University, Danang, 55000, Vietnam*

† Electronic supplementary information (ESI) available: Description of the characterization, electrochemical test, preparation of the gel electrolyte (PVA/KOH), asymmetric and symmetric device fabrication, comparison of the electrochemical activity of the CC-1-3 electrodes and other popular MOF-based electrodes in previous reports. See DOI: https://doi.org/10.1039/d5na00019j

MOFs represent an innovative class of hybrid materials with potential applications in carbon capture and storage, sensing, separation, and catalysis. Typically, MOFs are synthesized at the laboratory scale using organic solvent-based methods. However, this method poses significant environmental concerns and incurs high operational costs, hindering the large-scale production and applications of MOFs. A more sustainable and cost-effective alternative is the aqueous synthesis of MOFs, which avoids the use of organic solvents and mitigates these issues.[9] MOFs have garnered considerable attention as electrode materials for energy conversion and storage due to their high porosity and exceptional structural flexibility. These characteristics make MOFs increasingly interesting for a variety of energy-related applications. However, despite some MOFs achieving high operating voltages, their practical use is often restricted by their comparatively small capacitance. Recent research studies have shown the promise of MOF-M (where M can be metal ions such as Mg^{2+}, Mn^{2+}, Ni^{2+}, Co^{2+}, Zn^{2+}, Cu^{2+}, *etc.*) in synthesizing composite materials, owing to the presence of one or more metal centers within the framework.[10–15] Moreover, progress has been made in the direct carbonization of bimetallic MOFs, resulting in the formation of mixed oxides within a nanoporous carbon framework. This technique can be viewed as an alternative method for generating metal oxides. However, the extended preparation process of MOF-derived materials hampers their practical utility. Additionally, the calcination process unavoidably disrupts the MOF framework to some extent and diminishes the number of redox-active spots, thereby lowering the pseudocapacitive feature. MOFs have the potential to serve as electrodes by incorporating electrochemical redox sites. However, their inferior conductivity and stability currently limit their direct use as supercapacitor electrodes, preventing them from realizing their full potential.

Addressing the aforementioned issues, the most straightforward approach involves incorporating a secondary component to fabricate composite materials. This strategy enhances the electrical conductance and stability of the electrode by leveraging the synergetic interaction between the two constituents. For instance, Gholipour-Ranjbar *et al.*[16] described the development of a Ni–Co MOF using terephthalic acid and pyrazine as ligands *via* a hydrothermal method. This represents the first instance of this bimetallic MOF material being directly utilized as an electrode for SCs. The structure revealed that the metal centers were composed of Co^{2+} and Ni^{2+} ions. The specific capacitance of the Ni–Co MOF reached 1049 F g^{-1}, with the capacitance retaining 97.4% of its original value over 5000 trials. This result demonstrates the potential of bimetallic MOFs as candidates for supercapacitor applications. In another study, Zaka *et al.*[17] developed a Fe–Mg MOF using a step-wise synthetic procedure, followed by a hydrothermal process. The Fe–Mg MOF achieved a capacitance of 1825 C g^{-1} at 1.2 A g^{-1}, which is 1.59 and 1.31 times higher than that for the individual Fe and Mg MOFs, respectively. This electrode-based asymmetric device possesses the highest ED (57 W h kg^{-1}) and PD (2393 W kg^{-1}), which is credited to the synergetic effect of the DM-MOFs. Wang *et al.*[18] developed a single-step solvothermal process to create a Ni-MOF prototype for making a flower-like Ni–Co MOF through an *in situ* etching process. This electrode delivered a large capacity of 108.5 mA h g^{-1} at 0.5 A g^{-1}. The assembled asymmetric device achieved an ED of 45.7 W h kg^{-1} at a PD of 450.6 W kg^{-1} with a capacity retention of 84.3% over 6500 runs. This remarkable electrochemical activity is credited to the multi-stacked nanowire flower morphologies. Wang *et al.*[19] devised a hydrothermal method to fabricate combined 1D/3D cuboids of the Ni–Co MOF. This electrode showed the highest capacitance of 991 F g^{-1} at 1 A g^{-1}, alongside reduced intrinsic resistance and ion diffusion impedance, indicating its superior charge storage capability and enhanced electrochemical performance. Liang *et al.*[20] synthesized a Ni–Co MOF hydrothermally, featuring a layer/channel structure, which displayed commendable capacitive performance. This electrode revealed a capacitance of 1333 F g^{-1} at 2 A g^{-1}, with 83% of the original capacitance retained at 10 A g^{-1}. The constructed asymmetric devices achieved an ED of 28 W h kg^{-1} at 444 W kg^{-1} for an optimized Ni/Co ratio of 1 : 1. These findings underscore the enhanced stability and performance of bimetallic MOFs, attributed to the distinctive "interactions" or "dual-functional mechanism" arising from the interaction between the two distinct metal elements.

The construction of MOFs starts with selecting a synthesis procedure suitable for the envisioned use. MOFs are created by combining a metal salt with an organic ligand, characteristically composed of metal nodes and organic linkers under specific forms to attain the anticipated structure. In this study, we examined the influence of different synthetic procedures on the formation of heterostructures in bimetallic Cu/Co-MOFs and their electrochemical storage performance. Three distinct synthetic techniques, including step-by-step, single-step, and simple mixing, were employed to assess their impact. We found that the step-by-step synthesis method was more favorable for forming core–shell heterostructures compared to the single-step or simple mixing procedures. The CC-1 electrode demonstrated superior electrochemical performance compared to samples derived from other approaches. Leveraging these results, we assembled and compared the electrochemical storage properties of asymmetric and symmetric coin cell devices. As anticipated, the asymmetric supercapacitor device exhibited higher energy and power storage properties than the symmetric device.

2. Experimental details

In the step-by-step process, the linker solution was prepared by dissolving 4 grams of 2-methyl imidazole in 240 mL of methanol as the buffer solution, and the mixture was stirred continuously at 50 °C. A cobalt nitrate solution was prepared by dissolving 3.5 g of $Co(NO_3)_2 \cdot 6H_20$ in 240 mL ethanol. This was slowly added dropwise and mixed thoroughly with the above linker solution. Similarly, a copper nitrate solution was prepared with 4.5 g of $Cu(NO_3)_3 \cdot 3H_2O$ in 240 mL methanol. This too was added dropwise to the above solution, resulting in a cobalt linker solution. The final solution was mixed thoroughly for 120 min, and then washed with methanol. The black color precipitates were obtained in the wet form after discarding the

retentate. A dry powder was obtained after overnight drying at 80 °C; this step-by-step approach was labeled as CC-1. In the simple mixing process, 500 mL of linker solution was prepared and kept under stirring conditions. Cobalt and copper solutions were added dropwise simultaneously into the linker solution at 50 °C. The resultant solution was centrifuged, and the dried solid part was labeled as CC-2 MOF. Finally, the synthesized cobalt and copper MOFs were mixed in equal proportion, and ground with a stone mortar as a part of simple mixing process. The subsequent mixture was maintained at 200 °C for over 12 h, and the final product was denoted as CC-3 MOF. Details of the samples testing and electrochemical testing procedures are presented in the ESI file.†

3. Results and discussion

The methodology utilized for synthesizing CC-1, CC-2, and CC-3 MOFs, detailing the sequential and mechanistic steps in their formation, is outlined in Fig. 1. Subsequent to the hydrothermal synthesis, the resultant solid precipitates were systematically harvested through filtration. These samples were synthesized successfully, employing a sequential series of steps to attain distinct morphologies, facilitated by the 2-methylimidazole ligand. The XRD characteristic peaks observed in the diffraction patterns of the bare Cu MOF, Co MOF, and bimetallic CC-1, CC-2 and CC-3 samples are shown in Fig. 2. The Cu MOF showed a prominent XRD diffraction peak at 11.64°, corresponding to the (222) plane, which indicates a high level of crystallinity and matches CCDC-112954.[17] Likewise, the Co MOF displayed sharp diffraction peaks corresponding to CCDC-921721, demonstrating its crystalline structure.[21] In the case of hybrid samples, all these samples exhibit a prominent characteristic peak at 12.84° with high intensity, along with additional peaks at 25.76°, 35.4°, and 42.18°. While each sample exhibits

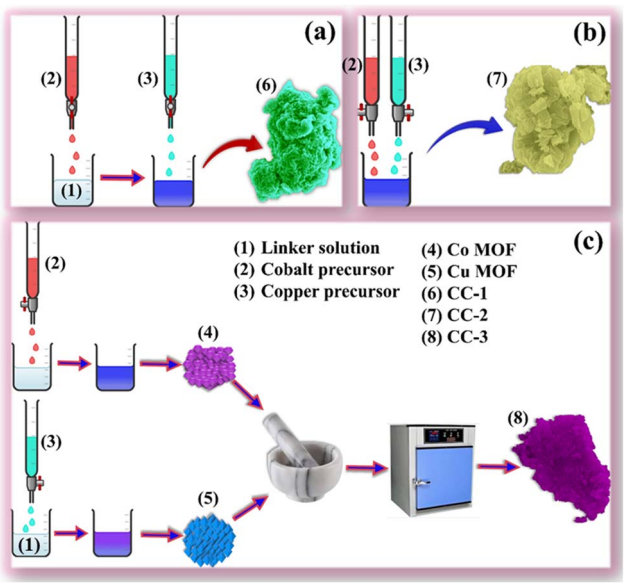

Fig. 1 Schematic of the material synthesis of (a) CC-1, (b) CC-2, and (c) CC-3.

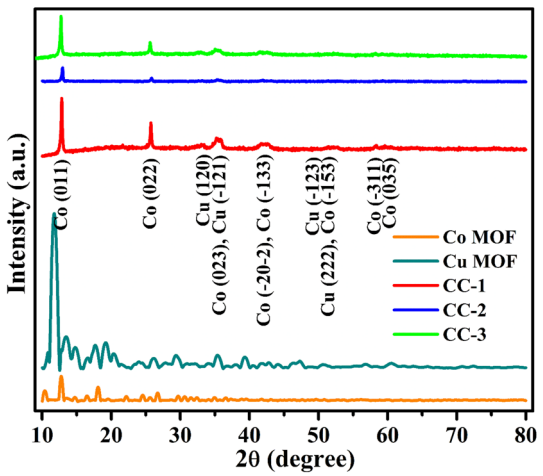

Fig. 2 XRD spectrum of Co MOF, Cu MOF, CC-1, CC-2, and CC-3.

a superposition of Co and Cu diffraction peaks, CC-1 MOF displays more pronounced intensities, suggesting a more defined crystalline structure. The observed (011), (022), (023), (−20−2), (−133), (−153), (−311), and (035) diffraction planes correspond to cobalt, while the (120), (−121), (−123), and (222) planes are attributed to copper, thereby confirming the effective integration of both materials. The deviation of the peaks from those of the pure constituents indicates the absence of isolated Cu MOF or Co MOF phases within the composite, further emphasizing the formation of a novel hybrid material.

Fig. 3 presents the FTIR spectra for the bare Cu MOF, Co MOF, and CC-1, CC-2, and CC-3 samples, and all samples were

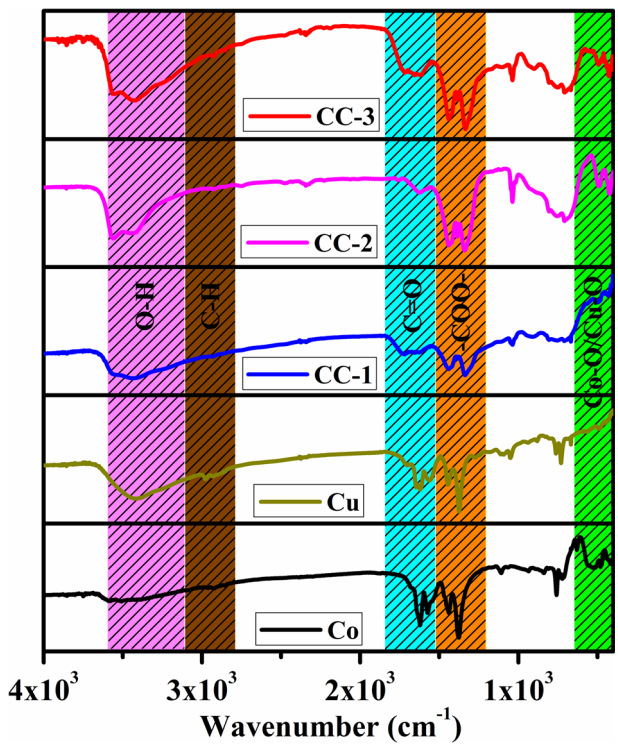

Fig. 3 FTIR spectra of Co MOF, Cu MOF, CC-1, CC-2, and CC-3.

synthesized using a 1 : 1 molar ratio of metal ions. For both Cu MOF and Co MOF, the C–H stretching modes are attributed to the relatively weak absorption bands between 2750 and 3100 cm^{-1}, while a broad O–H peak is observed in the 3100–3600 cm^{-1} range. Strong absorption knocks linked to the asymmetric and symmetric vibrations of C=O bonds appear in the 1530–1700 cm^{-1} region. Also, bands in the 400–600 cm^{-1} range are attributed to Co–O and Cu–O interactions.[21–23] These peaks indicate the effective integration of the ligand into the MOF structure. Additionally, the bands appearing between 1250 and 1500 cm^{-1} are associated with the carboxylic acid groups of the metallic ions, confirming the coordination of the metal ions within the MOF framework.[13,21] The interaction between the metal ions and water molecules is evident from the strong vibrational bands observed in the 3300–3500 cm^{-1} range, as well as between 700–770 cm^{-1}. These bands are consistent across all samples, suggesting that the coordination of the metal ions with water molecules is a common feature in the synthesized MOFs. The spectral similarities among CC-1, CC-2, and CC-3 reflect the consistency in their structural composition, despite any variations in synthesis conditions. This consistency in the FTIR spectra supports the hypothesis that the key structural features of these MOFs are preserved across different samples, which is critical for ensuring reproducibility and reliability in their electrochemical performance.

As depicted in Fig. 4, the CC-1 sample exhibits a core–shell flower-like structure, characterized by a Co core enveloped by blended petals arranged in a flower shape. In contrast, the CC-2

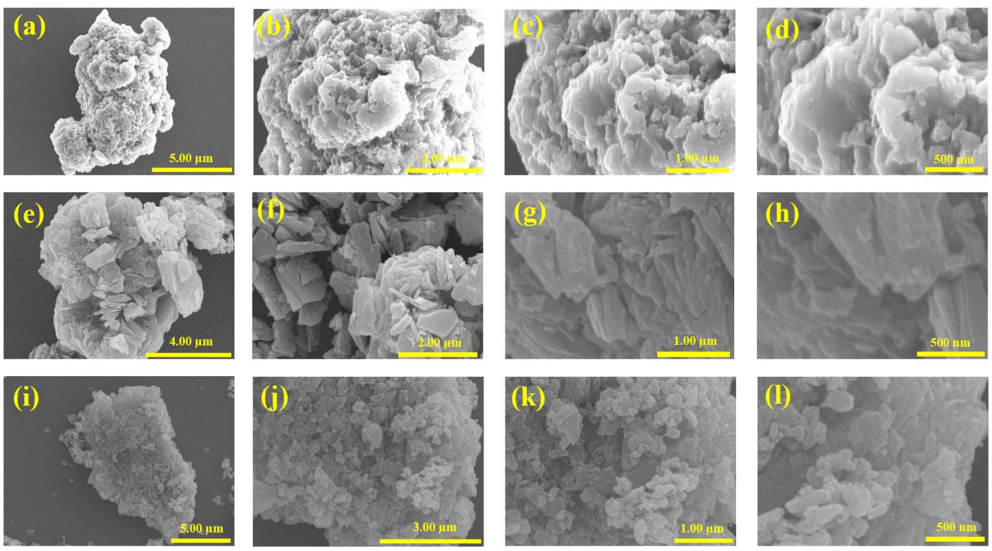

Fig. 4 SEM images of (a–d) CC-1, (e–h) CC-2, and (i–l) CC-3.

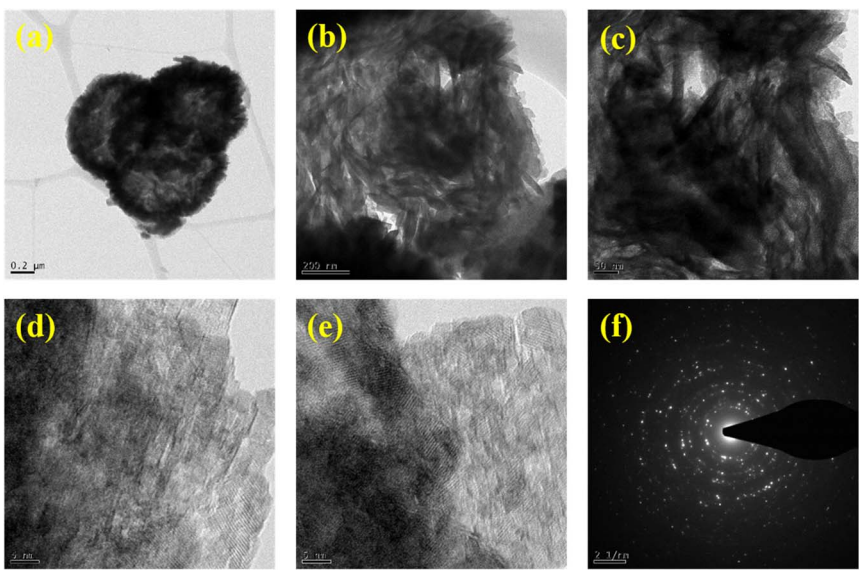

Fig. 5 (a–e) HR-TEM images of CC-1 and (f) SAED pattern.

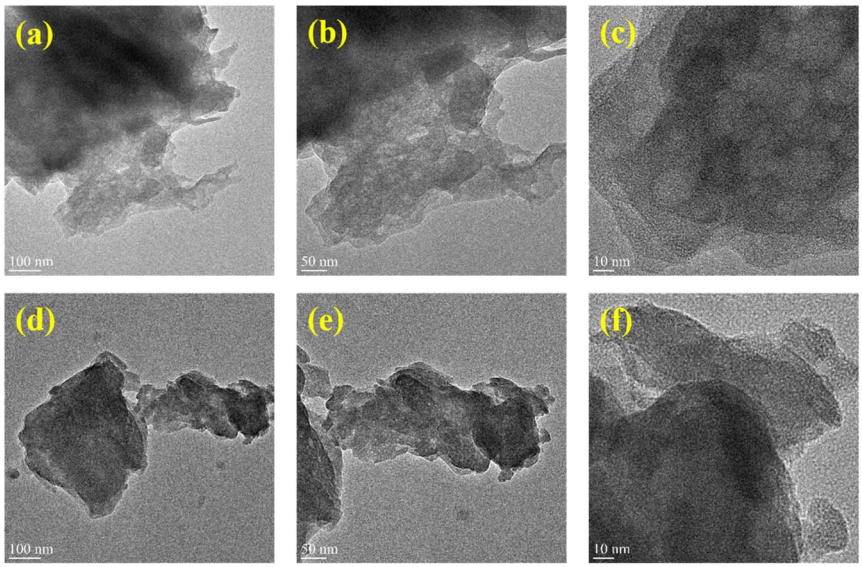

Fig. 6 HR-TEM images of (a–c) CC-2 and (d–f) CC-3.

and CC-3 samples feature irregular sheet-like shaped lamellar stacking structures. This stands in contrast to CC-1, which showcases octahedral crystals with minimal surface defects. Fig. 5 displays the HRTEM images of the CC-1 sample, while the HRTEM images of the CC-2 and CC-3 samples are illustrated in Fig. 6. The CC-1 samples showcase a core–shell flower-like structure characterized by curved petals with relatively high crystallinity. The lattice fringes of CC-1 are notably distinct compared to those of CC-2 and CC-3. Furthermore, the SAED pattern of CC-1 consists of a partial ring and dot pattern, suggesting the semi-crystalline nature of the core–shell structure. In contrast, CC-2 and CC-3 exhibit relatively low crystallinity due to their synthetic procedures. These findings indicate that the step-by-step approach (CC-1) yields attractive morphologies, potentially facilitating rapid ion transport due to the abundance of active edge sites.

Based on the preceding analysis, CC-3 was excluded from further consideration. Instead, the focus was shifted to a more detailed investigation of CC-2 and CC-1. This investigation involved examining their surface areas and pore size distributions using BET/BJH methods. The resulting data for these analyses are depicted in Fig. 7(a) and (b). Fig. 7a displays the BET isotherms for both CC-1 and CC-2, which are characterized as type IV isotherms. This categorization signifies that the materials are mesoporous, with pore diameters ranging from 2 to 50 nanometers. The BJH pore size distribution, illustrated in Fig. 7b, corroborates this classification by showing a similar range of pore sizes. In terms of quantitative surface area, CC-1 exhibits a higher value at 15.36 $m^2\ g^{-1}$ compared to CC-2, which has a surface area of 14.49 $m^2\ g^{-1}$. This difference in surface area suggests that CC-1 may have superior performance characteristics relative to CC-2, potentially due to the larger available surface area for interactions. Based on the results from the BET-BJH analysis, further investigations focused solely on CC-1. HRTEM mapping (Fig. 7c–h) reveals the occurrence of Co, Cu, C, O, and N constituents in CC-1, providing strong evidence for the formation of a mixed phase of Co–Cu MOF. These findings confirm that the CC-1 materials contain both Co and Cu elements. The incorporation of Cu into the Co MOF arrangement effectively hinders the crystal progression of Co MOF, leading to the formation of a unique microstructure in this bimetallic MOF system. The coexistence of core–shell flowers composed of curved petal-like lamellar structures in CC-1 potentially results in a more loosely packed stacking structure. This characteristic may be advantageous for the energy storage process. The estimated elemental concentration of Cu, Co and O is 38.26 wt%, 42.49 wt% and 19.23 wt%, respectively.

XPS testing was also conducted to explore the elemental configuration and valence state of the as-prepared CC-1. In the XPS complete spectra (Fig. 8a), characteristic peaks corresponding to Co, Cu, O, N, and C elements are observed. Moreover, the energy bands of Cu 2p, Co 2p, O 1s, N 1s, and C 1s were analyzed using the Gaussian system. The Co 2p peak is deconvoluted into 4 peaks (Fig. 8b), with dual peaks at 781.13 eV and 796.95 eV attributed to the $2p^{3/2}$ and $2p^{1/2}$ of Co^{2+}, respectively, signifying the bivalent state of the Co component in the CC-1 system.[24] The two additional peaks may represent satellite peaks of CC-1. The Cu 2p peak of CC-1 potentially exhibits four peaks, among which the sharp spikes at 954.56 eV and 934.59 eV correspond to the $2p^{1/2}$ and $2p^{3/2}$ of Cu^{2+},[25] respectively, indicating the bivalent state of the Cu component in CC-1 (Fig. 8c). These outcomes indicate that the Co and Cu components together preserve a bivalent state, while a complex interface amid Co^{2+}/Cu^{2+} and 2MI occurs in the CC-1 system. The C 1s peak of CC-1 was deconvoluted into three peaks at 288.11 eV, 285.88 eV, and 284.54 eV, matching to C–N, C=N, and C=C characteristic peaks, respectively (Fig. 8d).[26] The attendance of oxygen (O) in the graph is likely due to material oxidation upon exposure to air (Fig. 8e). The peak at 406.65 eV indicates the N 1s state of nitrogen (Fig. 8f).[27] The peaks observed in Fig. 8(d–f)

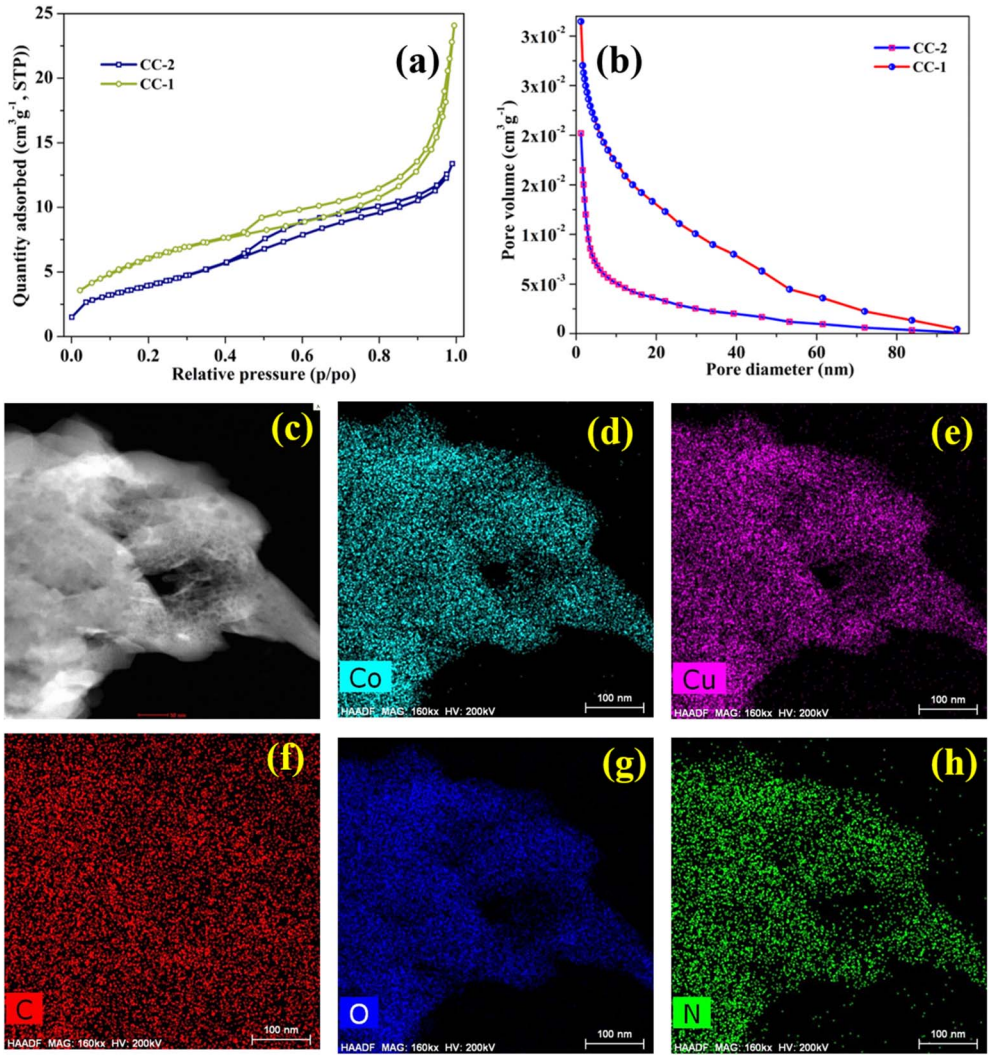

Fig. 7 (a) BET nitrogen adsorption–desorption isotherm, (b) BJH pore size distribution curve for CC-1 and CC-2, and (c–h) compositional elemental mapping of CC-1.

confirm the presence of C, O, and N in their 1s state. This finding is consistent with the results from the elemental mapping, which are illustrated in Fig. 7(f–h). The elemental mapping clearly shows the distribution of these elements, further validating their co-existence within the material.

As seen in Fig. 9a–c, the CV graphs of CC-1, CC-2, and CC-3 were obtained at different scan rates. Each CV curve demonstrations a pair of distinct redox peaks, indicating that the capacitive property of the Co–Cu MOF electrode is typical pseudo capacitance. As the sweep rates increase from 1 to 20 mV s^{-1}, the intensity of the redox spikes in all CV graphs of CC-1 and CC-3 increases while maintaining good shape. These peaks change to more positive and negative potentials, likely due to the interior resistance of the electrodes. For the CC-1 sample, two redox peaks appear at specific voltages (0.337 V and 0.476 V), similar to those observed in the CC-3 sample. However, the oxidation peak positions in CC-1 are shifted to higher values compared to CC-3, which can be attributed to the incorporation of Cu ions into the Co MOF. Fig. 9d compares the CV graphs of the bare Cu MOF, Co MOF, and CC-1, CC-2, and CC-3 electrodes at a particular scan rate (20 mV s^{-1}). All electrodes display a couple of distinctly divided faradaic redox peaks in the potential range of 0–0.6 V, indicating the incidence of reversible faradaic redox responses. Of all the electrodes, the CC-1 electrode exhibits the highest current density, indicating stronger pseudocapacitive properties compared to the bare Cu MOF and Co MOF electrodes. This indicates a lower degree of polarization and a high rate of ion transport at the surface compared to the other electrodes.[28] This is further supported by the calculated *b* value in the subsequent charge storage mechanism analysis. With the greatest integrated curve area and maximum current values, the CC-1 electrode achieves superior areal capacitance.

To further explore the electrochemical performance of CC-1, CC-2, and CC-3, GCD assessments at adjustable CDs were conducted, as shown in Fig. 10a–c. Even at high CDs, the GCD curves preserve a good shape, demonstrating the excellent rate capability. In alignment with the CV curve results, the GCD data

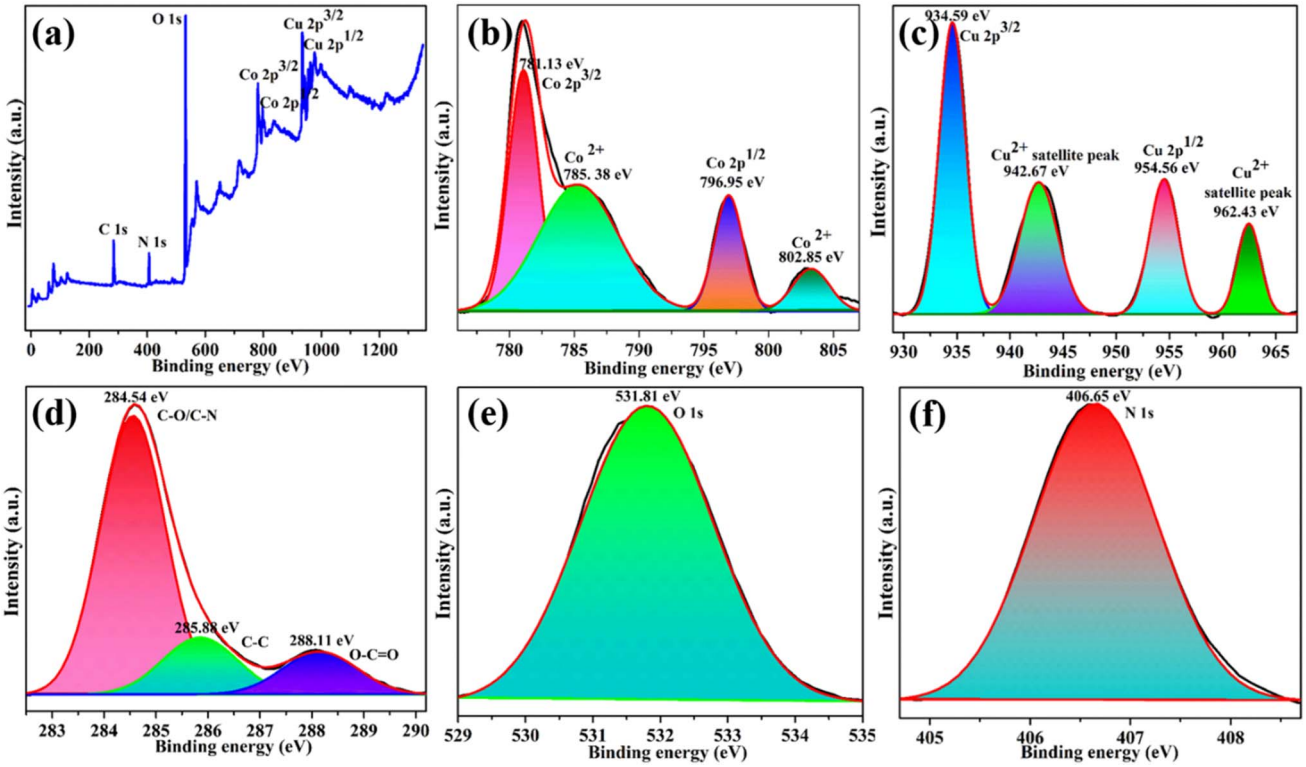

Fig. 8 High-resolution XPS spectrum (a), and XPS survey spectra: (b) Co 2p, (c) Cu 2p, (d) C 1s, (e) O 1s, and (f) N 1s.

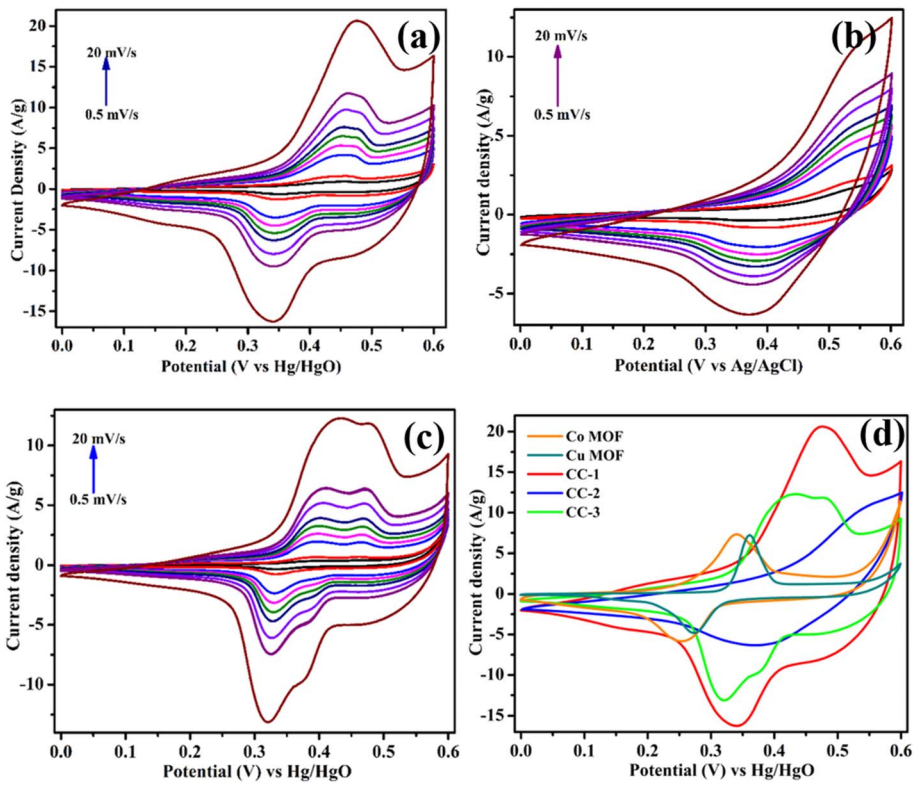

Fig. 9 CV curves of (a) CC-1, (b) CC-2 [reprintted with permission from ref. 28 © Elsevier (2025)], and (c) CC-3 for the three-electrode system, and (d) the comparison of the CV curves @ 20 mV s^{-1}.

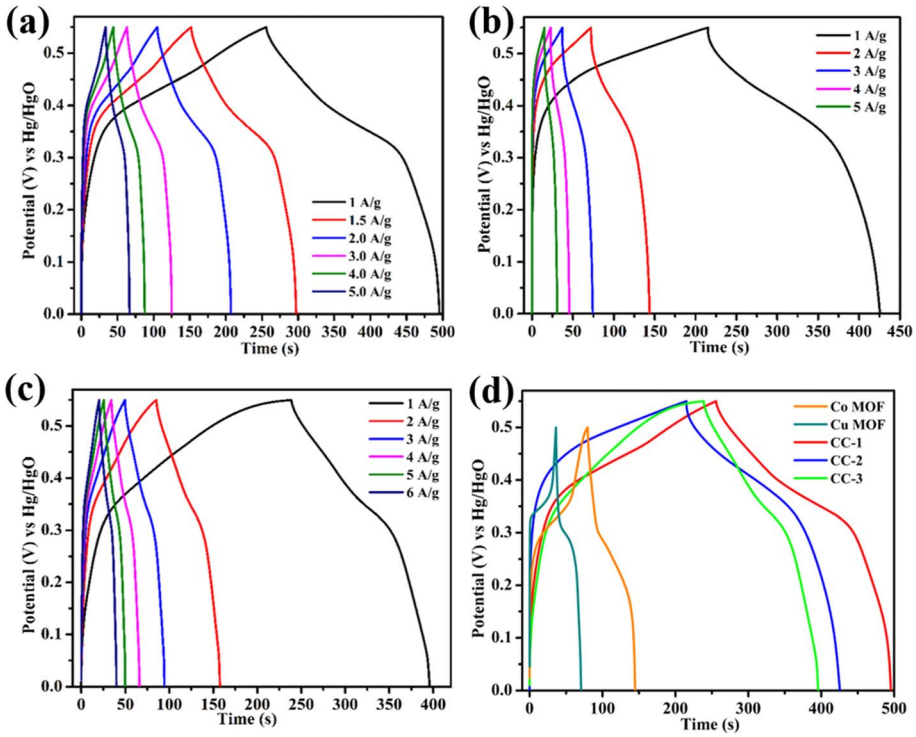

Fig. 10 GCD curves of (a) CC-1, (b) CC-2 [reprintted with permission from ref. 28 © Elsevier (2025)], and (c) CC-3 for the three-electrode system, and (d) the comparison of the GCD curves @ 1 A g^{-1}.

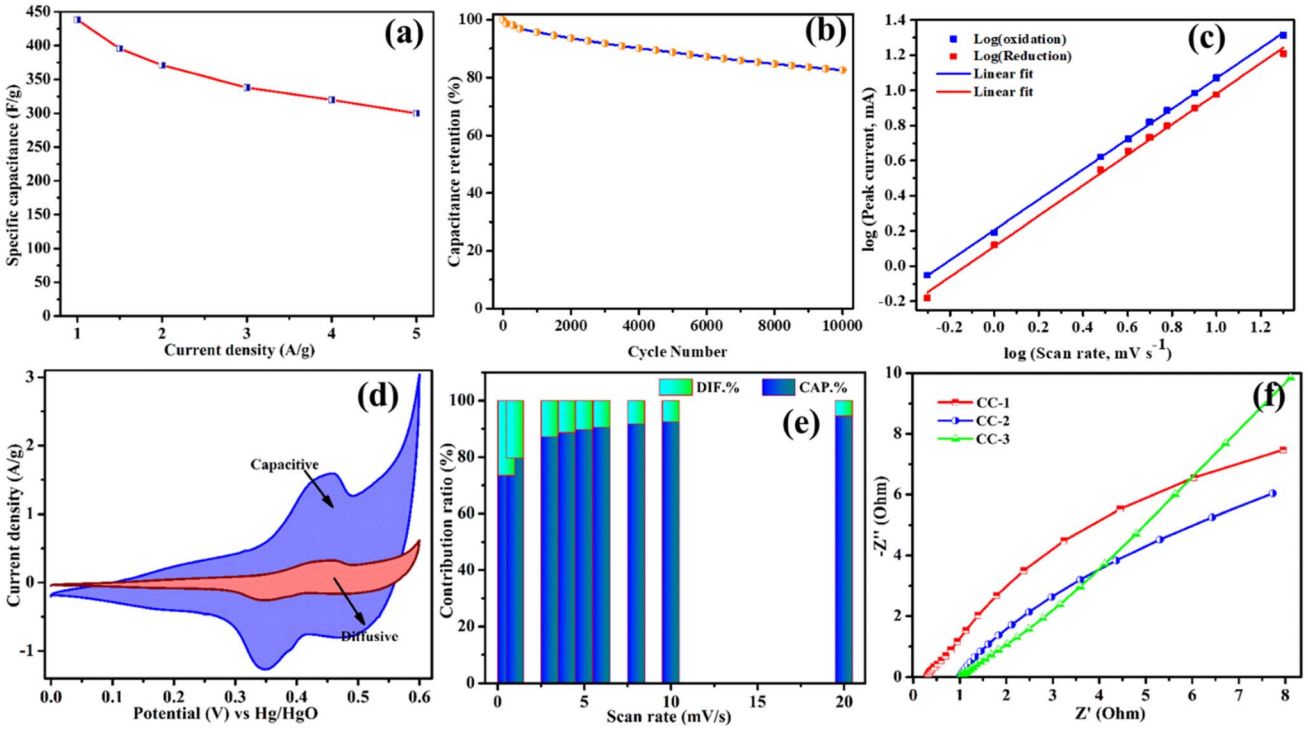

Fig. 11 (a) Specific capacitance variation with current density. (b) Capacitance retention tested for 10 000 cycles. (c) Logarithmic relation between the oxidation and reduction peak currents with the scan rate. Capacitive and diffusion-controlled energy storage contribution of CC-1 (d) in the form of a CV curve and (e) at various scan rates from 0.5–20 mV s^{-1} (f) EIS spectra of CC-1, CC-2, and CC-3.

for the bare Cu MOF, Co MOF, and CC-1, CC-2, and CC-3 electrodes, shown in Fig. 10d, demonstrate that CC-1 delivers a longer discharge time at 1 A g^{-1} compared to the other electrodes. Thus, the specific capacitance of the electrodes follows the order of CC-1 > CC-2 > CC-3. The gradually decreasing discharge graph, reflecting the broad redox peaks in the CV curves, further proves the pseudocapacitive characteristics of the CC-1 electrode.

Fig. 11a illustrates the capacitance *versus* CD for the CC-1 electrode. At CD of 1, 1.5, 2, 3, 4, and 5 A g^{-1}, the specific capacitance of CC-1 reaches 438, 395, 371, 338, 320, and 300 F g^{-1}, respectively. Fig. 11b displays the cycling stability of the CC-1 electrode, revealing an impressive capacitance retention rate of 82.5% over 10 000 runs. This underscores the exceptional electrochemical performance of the CC-1 electrode, which is attributed to its distinctive core–shell, flower-like structure and high crystallinity, supporting the efficient ion transport and boosted pseudocapacitive features. The incorporation of Cu ions into the Co MOF framework plays a key role by restricting crystal growth and generating a loosely packed structure, which is advantageous for energy storage.

The reaction rates for the energy storage system were further investigated using CV graphs based on the power law. As presented in Fig. 11c, the *b* value for CC-1 is approximately 0.86, which falls within the range of 0.5 to 1.0. This indicates that both surface-controlled and diffusion-controlled processes influence the reaction kinetics, suggesting that the CC-1 electrode exhibits a combination of pseudocapacitive behavior. The core–shell structure of CC-1 significantly enhances the surface-controlled influence on the charge storage progression, which in turn enables improved rate performance. Fig. 11d presents the CV curves separating the capacitive and diffusive contributions for CC-1. The data reveal that the capacitive influence is more dominant than the diffusive-controlled influence, emphasizing that the primary storage mechanism is based on pseudo-capacitance. This dominance of the capacitive behavior suggests that the core–shell architecture of CC-1, with its extraordinary surface area and abundant active centers, plays a vital role in the efficient and rapid charge storage progression. Moreover, the structural attributes of CC-1, such as its core–shell flower-like morphology and high crystallinity, contribute to the enhanced electrochemical performance. These features not only deliver a larger vigorous surface area for redox reactions but also ensure better ion diffusion pathways, thereby improving the overall energy storage efficiency. The incorporation of Cu ions into the Co MOF-framework constrains excessive crystal growth, ensuring a more loosely packed structure that is beneficial for energy storage. The combination of these factors (*i.e.*, unique morphology, high crystallinity, and synergy effects of the bimetallic composition) positions CC-1 as a superior electrode material with excellent rate capability and enhanced pseudocapacitive behavior. These attributes make it a capable candidate for high-performance energy storage uses, offering significant advantages over other materials tested in this study.

For the CC-1 electrode, the influence from surface/capacitive-controlled capacity rises with the sweep rate, as shown in Fig. 11e. As the sweep rate rises, the diffusion-organized intercalation/de-intercalation contribution decreases. This indicates that at higher scan rates, the total capacity is controlled by surface capacitance, which is likely due to the rapid charge–discharge developments. Similar behavior has been observed in other studies involving bimetallic MOFs, demonstrating that the scan rate significantly impacts the charge storage process. To further analyze the charge transport kinetics of the CC-1, CC-2, and CC-3 electrodes, EIS was conducted. The EIS results, depicted in Fig. 11f, show the impedance curves with varying grades in the small-frequency zone, indicating the diffusive actions of the electrolytes. Consistent with its huge capacitance, CC-1 reveals a low solution resistance (R_s) value of 0.275 Ω, suggesting efficient ion transport to the electrode. In contrast, the CC-2 and CC-3 electrodes have higher R_s values of 0.93 Ω and 0.98 Ω, respectively, indicating more resistance to ion transport. Moreover, the Nyquist plots for CC-1 feature an incomplete semicircle. This signifies that the electrolyte and electrode are very wettable, and that the electron transport across the interface is rapid during electrochemical progressions. This fast electron transfer rate contributes to the advanced electrochemical activity of CC-1, as it enhances the efficiency of the charge storage and retrieval processes. The enhanced performance of CC-1 can be ascribed to its unique core–shell flower-like structure, which offers an enormous active surface area and ample active centers for redox reactions. This structure not only facilitates rapid ion diffusion, but also ensures a more efficient charge storage mechanism dominated by surface capacitance at higher scan rates. The combination of low R_s values, fast interfacial electron transfer, and a structure that promotes rapid ion diffusion underscores the advantages of the CC-1 electrode. These features make it a highly promising candidate for high-performance energy storage uses, outperforming CC-2 and CC-3 in terms of capacitance, charge transport kinetics, and overall electrochemical behavior. The superior electrochemical performance of CC-1 compared to other samples can be credited to several factors. Firstly, the optimized concentration ratio of 1 : 1 for Co and Cu plays a significant role in enhancing the material's properties. Secondly, the unique core–shell flower-like morphology of CC-1 offers a superior surface area and further energetic sites, which facilitates better ion transport and electron conductivity. Lastly, the high activity of the open metal centers further boosts the material's electrochemical performance. These combined effects result in a remarkable synergy that enhances the overall efficiency and effectiveness of the CC-1 electrode in energy storage applications. The high electrochemical performance of the CC-1 supercapacitor electrode is credited to its synergistic bimetallic Co/Cu-based redox reactions, which enhance the charge storage through pseudocapacitive behavior and efficient ion transport, mainly:

$$Co^{2+} + 2OH^- \rightleftharpoons Co(OH)_2 + 2e^- \quad (1)$$

$$Cu^{2+} + e^- \rightleftharpoons Cu^+ \quad (2)$$

In summary, the enhanced electrochemical performance of CC-1, compared to CC-2 and CC-3, can be explained by the

following factors: (i) the CC-1 electrode ensures a balanced redox reaction, preventing excessive crystal growth and maintaining a highly active electrode surface, (ii) the unique hierarchical structure of CC-1 provides a large electroactive surface area, refining the electrolyte penetration and reducing charge diffusion resistance, (iii) the incorporation of Cu within the Co-MOF structure modulates crystallization, leading to a more open porous structure that boosts ion transport and charge storage, and (iv) the electrical chemical results indicate that CC-1 exhibits dominant pseudocapacitive behavior, with fast surface-controlled charge storage at high scan rates.

To assess the practical applications of the CC-1 electrode, the electrochemical progression of the built CC-1//AC and CC-1//CC-1 devices was investigated. Fig. 12a shows the individual CV graphs of two electrodes at 20 mV s^{-1}, indicating that the voltage windows of CC-1 and AC are 0–0.6 V and −1.0–0 V, respectively. To learn more about the CC-1//AC device's optimal operating voltage range, CV graphs were obtained across diverse prospective windows from 0.4 to 1.4 V at 50 mV s^{-1}, as presented in Fig. 12b. The CV graphs preserve a decent shape up to a voltage of 1.4 V, indicating the stability of the CC-1 electrode. Consequently, an operating voltage of 1.4 V was selected for subsequent electrochemical tests of the CC-1//AC device.

Fig. 12c shows the CV graphs of the CC-1//AC device at 2 to 400 mV s^{-1}, exhibiting a leaf-like shape that indicates good capacitive behavior. The resultant GCD graphs of the CC-1//AC device are shown in Fig. 12d, which demonstrates the charge–discharge characteristics of the device. Fig. 12e illustrates the specific capacitance *versus* current density of the CC-1//AC device. The CC-1//AC device brought a capacitance of 149.37 F g^{-1} at 1 A g^{-1}, outperforming previously reported devices such as Ni-CoMOF//rGO (113 F g^{-1}),[29] Ni-CoMOF//AC (97 F g^{-1} @ 0.5 A g^{-1}),[30] and Ni-CoMOF//AC (59 F g^{-1} at 1 A g^{-1}).[31] The Ragone graph of the CC-1//AC device, as shown in Fig. 12f, demonstrates an ED of 40.4 W h kg^{-1} at 302.37 W kg^{-1}. This performance surpasses previously reported devices such as NiO/

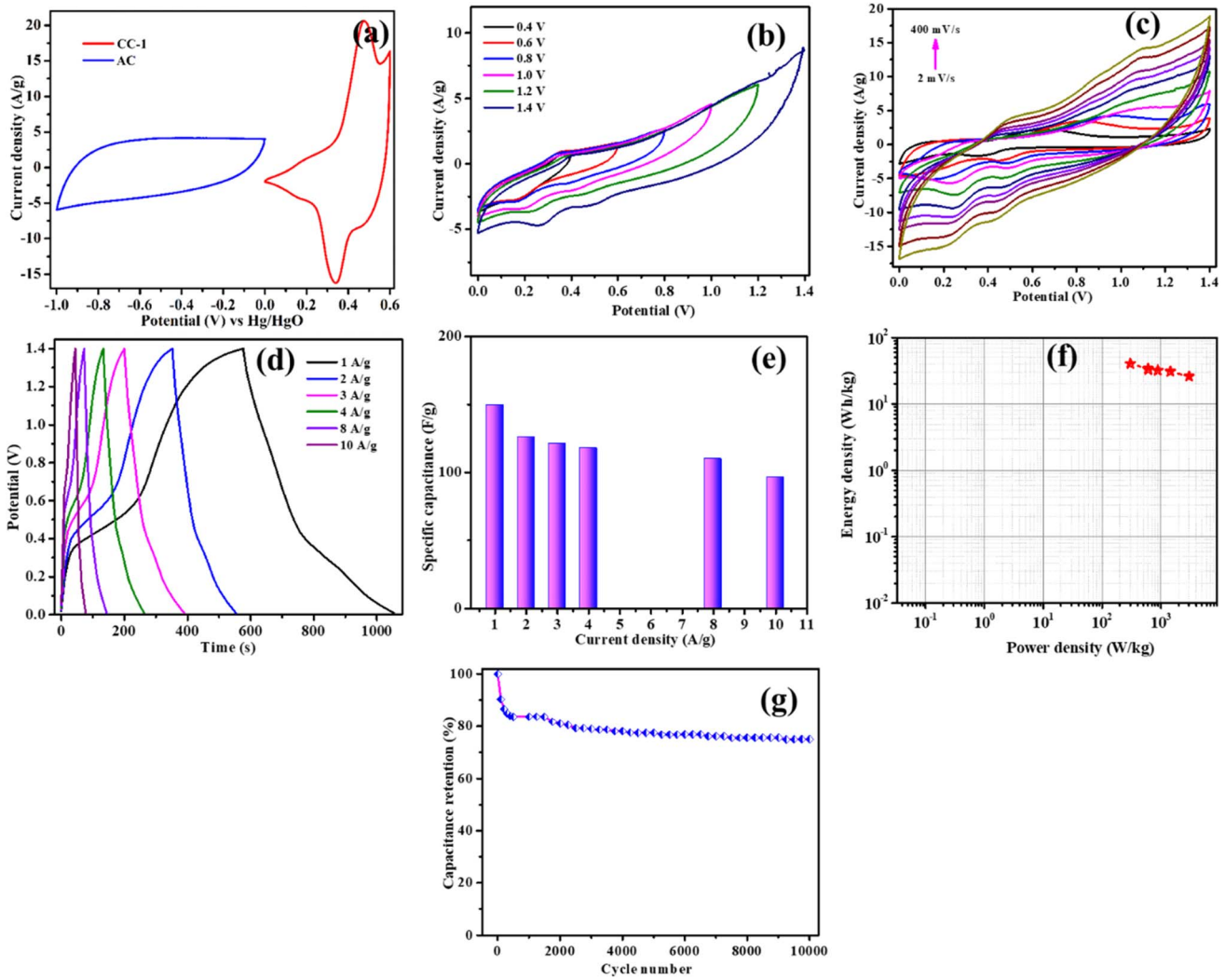

Fig. 12 (a) CV profiles of activated carbon and CC-1 MOF, (b) CV curves of the AC//CC-1 device for different potentials, (c) CV curves for the wide scan range of 2–400 mV s^{-1}, GCD curves (d), specific capacitance (e) at various current densities, (f) Ragone plots, and (g) capacitance retention over 10 000 cycles.

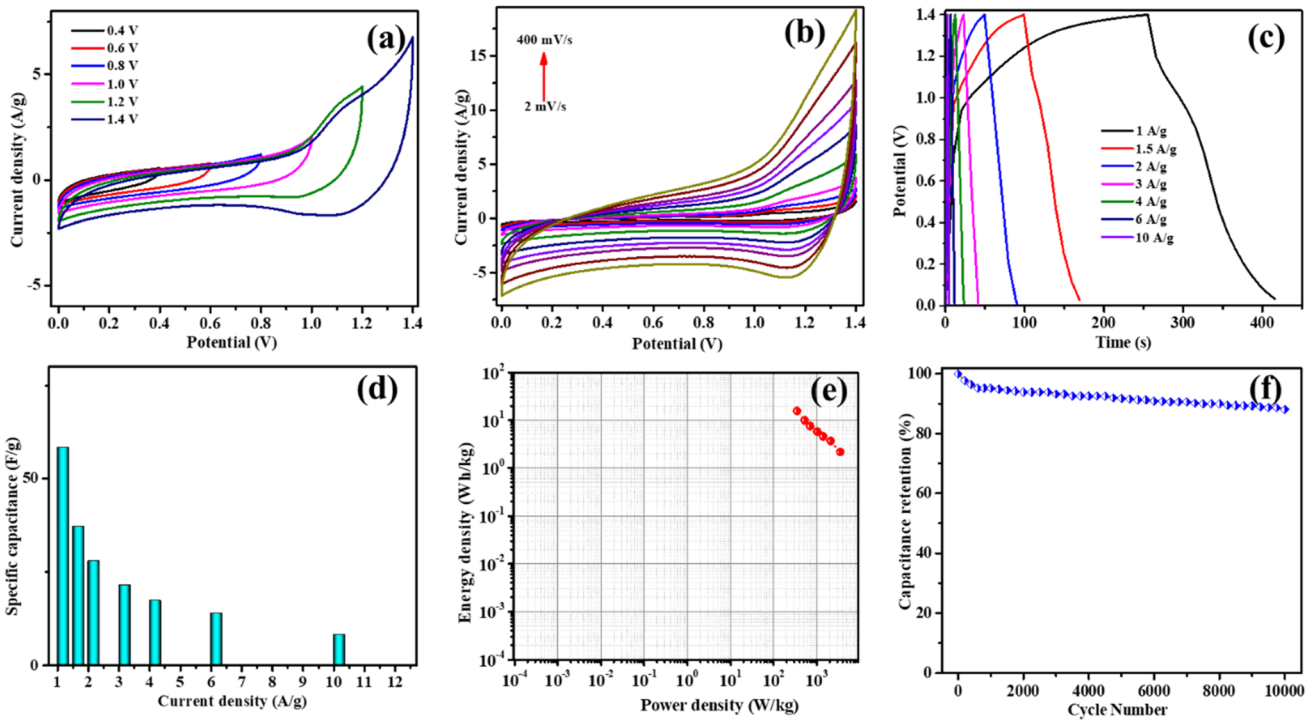

Fig. 13 (a) CV curves of the CC-1//CC-1 device for different potentials, (b) CV curves for the wide scan range of 2–400 mV s^{-1}, GCD curves (c), specific capacitance (d) at various current densities, (e) Ragone plots, and (f) capacitance retention over 10 000 cycles.

NiMOF//AC, which delivered 39.2 W h kg^{-1} at 700 W kg^{-1},[32] Co MOF//AC with 34.4 W h kg^{-1} @ 375.3 W kg^{-1},[33] Mo-NiMOF//AC achieving 59 W h kg^{-1} at 802.1 W kg^{-1},[34] and Co-MnMOF//AC with a performance of 30 W h kg^{-1} at 685 W kg^{-1}.[35] The enhanced performance of the CC-1//AC device can be attributed to its unique core–shell flower-like structure, which facilitates efficient ion transport and electron conductivity, resulting in improved energy and power densities. This exceptional performance highlights the potential of the CC-1 electrode in developing high-efficiency energy storage systems. Thus, the superior performance of the CC-1//AC device can be ascribed to the distinctive core–shell flower-like assembly of the CC-1 electrode. This distinctive morphology enhances the ion transport and electron conductivity, significantly improving both energy and power densities. More electrochemical reaction sites and a bigger surface area are both provided by the core–shell arrangement, facilitating faster ion diffusion and better charge storage. Additionally, the flower-like design helps to reduce the internal resistance, contributing to the overall efficiency of the device. This exceptional performance underscores the potential of the CC-1 electrode in developing high-efficiency energy storing systems, making it a capable candidate for future applications in advanced supercapacitors. The CC-1//AC device also demonstrated superior cycling stability (Fig. 12g), retaining as much as 75% of the initial capacitance after 10 000 prolonged cycles at a 12 A g^{-1}. This excellent electrochemical activity can be accredited to the unique core–shell flower-like structure of the CC-1 electrode, which delivers an enormous surface area and numerous active centers for redox reactions. The high crystallinity of CC-1 enhances the ion diffusion and electron transport, contributing to its high specific capacitance and exceptional cycling stability.

The impressive electrochemical performance of CC-1 in the three-electrode system paves the way for constructing a fully symmetrical supercapacitor cell. In this study, we assembled a symmetrical cell using two equally weighted CC-1 electrodes, separated by a gel electrolyte composed of KOH and PVA. The polymer gel electrolyte prevents the device from leaking by acting as both an electrolyte and a separator. Using a constant scan rate of 50 mV s^{-1}, we conducted CV analysis at several potential windows to find the ideal operating potential window. Fig. 13a displays the CV curves for various potential windows. The greatest current was obtained within the range of 0.4 to 1.4 V, similar to the CC-1//AC device. Fig. 13b displays the CV graphs in the range of 2 to 400 mV s^{-1}, showing a slight deviation from the non-rectangular form due to the pseudocapacitive nature of CC-1 observed in the three-electrode system. Fig. 13c presents the GCD graphs of the CC-1//CC-1 device, revealing a remarkable capacitance of 58.12 F g^{-1} at 1 A g^{-1} (Fig. 13d). This corresponds to ED of 15.7 W h kg^{-1} at PD of 346.7 W kg^{-1}, as presented in the Ragone graph in Fig. 13e.

The cycling stability of the CC-1//CC-1 device was evaluated over 10 000 cycles at 12 A g^{-1}, as shown in Fig. 13f. The device preserves 88% of its preliminary capacitance over 10 000 runs, indicating its potential for real-world applications. The performance of the CC-1//CC-1 device was compared to various symmetrical DM-MOFs, such as Ni-ZnMOF//Ni-ZnMOF (33.25 W h kg^{-1} at 900 W kg^{-1})[36] and Cu-MOF/rGO//Cu-MOF/rGO (30.56 W h kg^{-1} at 600 W kg^{-1}).[37] The CC-1//CC-1 device exhibits superior performance, showcasing its potential for

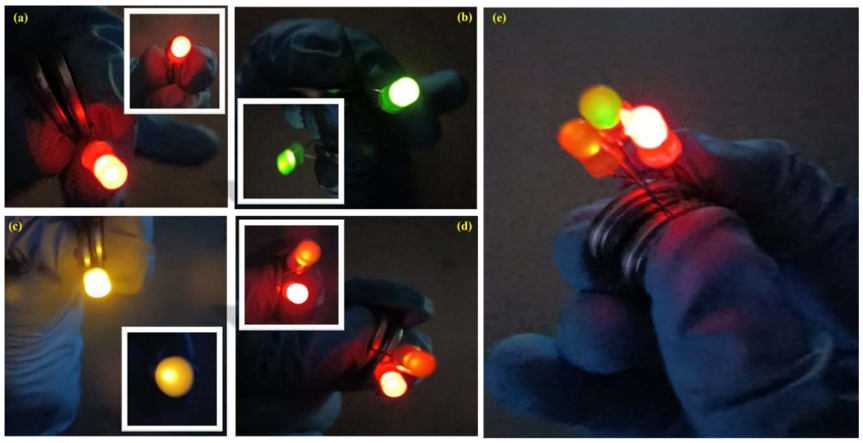

Fig. 14 Real-time power application of asymmetric devices coupled in series. Illumination of a red LED (a); green LED (b); yellow LED (c); simultaneous illumination of yellow and red LEDs (d); one-time illumination of red, green, and yellow LEDs (e).

high-efficiency energy storage systems. Furthermore, the practical application of the invented coin cell devices was demonstrated by powering red, green, and yellow LEDs. After being partially recharged, the devices showed an ultra-stable operating potential of 1.6 V. For the demonstration, two asymmetric devices were coupled in series to light the LEDs. Each LED was successfully illuminated for over 4 minutes, 2 minutes, and 1 minute for the red, green, and yellow LEDs, respectively. The testing continued with red and yellow LEDs connected in parallel, both of which also lit up successfully. Encouraged by these results, an attempt was made to light all three LEDs simultaneously. The successful operation of all three LEDs was documented and is presented in Fig. 14. The FESEM images of CC-1 (Fig. S1†) after the electrochemical stability test reveal that the electrode retains its initial morphological characteristics even after prolonged cyclic operations. The core–shell flower-like structure remains well-preserved, signifying the robustness of the material under repeated charge–discharge cycles. No significant structural degradation, fragmentation, or collapse of the porous framework is detected, demonstrating the high mechanical and electrochemical stability of CC-1. The interconnected porous network remains intact, certifying efficient ion transport and maintaining the electrode's performance over extended usage. These findings confirm the structural durability of CC-1, making it a reliable material for long-term supercapacitor uses.

4. Conclusion

In this study, we have explored various synthesis techniques and electrochemical behaviour of bimetallic MOFs with a focus on their application in supercapacitors. Specifically, the CC-1, CC-2, and CC-3 samples were synthesized using different methodologies, with CC-1 demonstrating superior performance due to its unique core–shell flower-like morphology and optimized concentration ratio of 1 : 1 for Co and Cu. The synthetic procedure for CC-1 involved a step-by-step approach that resulted in a distinctive morphology with high crystallinity, as evidenced by HRTEM and XRD analyses. The high crystallinity and unique structure of CC-1 facilitated enhanced ion transport and electron conductivity, contributing to its outstanding electrochemical performance. XPS analysis confirmed the successful integration of Co and Cu in the MOF structure, with both metals maintaining their bivalent states. The incorporation of Cu into the Co MOF system inhibited crystallization progress, leading to a loose stacking structure that was beneficial for energy storage. Electrochemical tests highlighted the pseudocapacitive behavior of CC-1, with redox peaks indicating the good capacitive properties. The GCD tests showed that CC-1 exhibited an extended discharge time and superior specific capacitance compared to CC-2 and CC-3, with excellent rate capability and cycling stability. Further analysis of the reaction kinetics revealed that the charge storage mechanism of CC-1 is controlled by surface-capacitive processes at high scan rates and efficient ion transport. The practical application of CC-1 was demonstrated by assembling a CC-1//AC device that exhibited high capacitance (341 F g^{-1}), excellent ED@PD (40.4 W h kg^{-1} @ 302.3 W kg^{-1}), and superior cycling stability (75%) compared to the CC-1//CC-1 device (58.2 F g^{-1}, 15.7 W h Kg^{-1} @346.7 W kg^{-1}). The unique core–shell flower-like structure of CC-1 was crucial in achieving these remarkable performance metrics.

Data availability

The data that support the findings of this study are available from the corresponding author (Dr Gyu Sang Choi) upon reasonable request.

Conflicts of interest

The authors declare no competing financial interests.

Acknowledgements

This work was supported by a National Research Foundation of Korea (NRF) grant funded by the Korea government (MSIT) (RS2023-00280665).

References

1 M. Ahmed, Recent advancement in bimetallic metal organic frameworks (M′MOFs): synthetic challenges and applications, *Inorg. Chem. Front.*, 2022, **9**, 3003–3033.
2 Yu Yang, Y. Ma, C. Lu, S. Li and M. Zhu, Molten salt technique for the synthesis of carbon-based materials for supercapacitors, *Green Chem.*, 2023, **25**, 10209–10234.
3 B. Zhang, X. Feng, R. Ma, R. Sheng, D. Wang, F. Chen, Y. Wang, M. Xu, L. Ai, N. Guo and L. Wang, Constructing the Interconnected and Hierarchical Nanoarchitectonics in Coal-Derived Carbon for High-Performance Supercapacitor, *Langmuir*, 2024, **40**, 13467–13475.
4 R. K. Pandey, Bimetallic metal–organic frameworks (BMOFs) and their potential applications, metal–organic frameworks for carbon capture and energy, *ACS Symposium Series*, 2021, vol. 1393, ISBN13: 9780841298088.
5 S. M. Benoy, A. Hazarika, M. Bora, A. Rajbongshi, D. Sarmah, M. K. Phukan and B. K. Saikia, Coal-Derived Porous Carbon as Versatile Electrode Materials for Aqueous, Water-in-Salt, and Organic Electrolytes, and Fabrication of Pouch Cell Supercapacitor toward Power Application, *ACS Appl. Energy Mater.*, 2024, **7**, 6045–6061.
6 X. Chu, F. Meng, T. Deng, Y. Lu, O. Bondarchuk, M. Sui, M. Feng, H. Li and W. Zhang, Mechanistic insight into bimetallic CoNi-MOF arrays with enhanced performance for supercapacitors, *Nanoscale*, 2020, **12**, 5669–5677.
7 M. Zhu, Y. Yang and Y. Ma, Salt-assisted synthesis of advanced carbon-based materials for energy-related applications, *Green Chem.*, 2023, **25**, 10263–10303.
8 J. Wang, J. Liang, Y. Lin, K. Shao, X. Chang, L. Qian, Z. Li and P. Hu, Nanowire stacked bimetallic metal–organic frameworks for asymmetric supercapacitor, *Chem. Eng. J.*, 2022, **446**, 137368.
9 N. Raza, T. Kumar, V. Singh and K. H. Kim, Recent advances in bimetallic metal–organic framework as a potential candidate for supercapacitor electrode material, *Coord. Chem. Rev.*, 2024, **430**, 213660.
10 Y. Liang, W. Yao, J. Duan, M. Chu, S. Sun and X. Li, Nickel cobalt bimetallic metal–organic frameworks with a layer-and-channel structure for high-performance supercapacitors, *J. Energy Storage*, 2021, **33**, 102149.
11 P. I. Scheurle, A. Mähringer, A. C. Jakowetz, P. Hosseini, A. F. Richter, G. Wittstock, D. D. Medina and T. Bein, A highly crystalline anthracene-based MOF-74 series featuring electrical conductivity and luminescence, *Nanoscale*, 2019, **11**, 20949–20955.
12 S. V. P. Vattikuti, J. Shim, N. Nguyen Dang, P. Rosaiah, M. R. Karim, I. A. Alnaser and B. Khan, Enhanced photocatalytic and electrochemical performance of MOF-derived NiO-ZnO oxide composites for wastewater treatment and sustainable energy storage, *Int. J. Energy Res.*, 2024, **2024**, 4589047.
13 J. Zeng, K. C. Devarayapalli, S. V. P. Vattikuti and J. Shim, Split-cell symmetric supercapacitor performance of bimetallic MOFs yolk–shell hierarchical microstructure, *Mater. Lett.*, 2022, **309**, 131305.
14 A. N. Hong, H. Yang, X. Bu and P. Feng, Pore space partition of metal–organic frameworks for gas storage and separation, *EnergyChem*, 2022, **4**, 100080.
15 J. Zeng, K. C. Devarayapalli, S. V. P. Vattikuti and J. Shim, Hierarchical 3D micro-nanostructures based on *in situ* deposited bimetallic metal–organic structures on carbon fabric for supercapacitor applications, *Int. J. Energy Res.*, 2021, **46**, 6031–6044.
16 H. Gholipour-Ranjbar, M. Soleimani and H. R. Naderi, Application of Ni/Co-based metal–organic frameworks (MOFs) as an advanced electrode material for supercapacitors, *New J. Chem.*, 2016, **40**, 9187.
17 A. Zaka, M. W. Iqbal, A. M. Afzal, H. Hassan, H. Rafique, S. M. Wabaidur, A. M. Tawfeek and E. Elahi, A bimetallic Fe–Mg MOF with a dual role as an electrode in asymmetric supercapacitors and an efficient electrocatalyst for hydrogen evolution reaction (HER), *RSC Adv.*, 2023, **13**, 26528–26543.
18 J. Wang, J. Liang, Y. Lin, K. Shao, X. Chang, L. Qian, Z. Li and P. Hu, Nanowire stacked bimetallic metal–organic frameworks for asymmetric supercapacitor, *Chem. Eng. J.*, 2022, **446**, 137368.
19 X. Wang, Q. Li, N. Yang, Y. Yang, F. He, J. Chu, M. Gong, B. Wu, R. Zhang and S. Xiong, Hydrothermal synthesis of NiCo-based bimetal–organic frameworks as electrode materials for supercapacitors, *J. Solid State Chem.*, 2019, **270**, 370–378.
20 Y. Liang, W. Yao, J. Duan, M. Chu, S. Sun and X. Li, Nickel cobalt bimetallic metal–organic frameworks with a layer-and-channel structure for high-performance supercapacitors, *J. Solid State Chem.*, 2021, **33**, 102149.
21 F. Arjmand and Z. R. Ranjbar, Impact of copper and cobalt-based metal–organic framework materials on the performance and stability of hole-transfer layer (HTL)-free perovskite solar cells and carbon-based, *Sci. Rep.*, 2024, **14**, 12843.
22 T. Chen, A. Yang, W. Zhang, J. Nie, T. Wang, J. Gong, Y. Wang and Y. Ji, Architecting nanostructured Co-BTC@GO composites for supercapacitor electrode application, *nanomaterials*, 2022, **12**, 3234.
23 B. Venu, V. Shirisha, B. Vishali, G. Naresh, R. Kishore, I. Sreedhar and A. Venugopal, A Cu-BTC metal–organic framework (MOF) as an efficient heterogeneous catalyst for the aerobic oxidative synthesis of imines from primary amines under solvent free conditions, *New J. Chem.*, 2020, **44**, 5972–5979.
24 A. R. P. Santiago, S. A. Tolba, M. A. Ahsan, O. Fernandez-Delgado, M. S. Adly, E. M. Hashem, M. M. Abodouh, M. S. El-Shall, S. T. Sreenivasan, N. K. Allam and L. Echegoyen, Co−Cu bimetallic metal organic framework catalyst outperforms the Pt/C benchmark for oxygen reduction mohamed fathi sanad, *J. Am. Chem. Soc.*, 2021, **143**, 4064–4073.

25 H. Li, S. Xu, J. Du, J. Tang and Q. Zhou, Cu@Co-MOFs as a novel catalyst of peroxymonosulfate for the efficient removal of methylene blue, *RSC Adv.*, 2019, **22**, 9410–9420.
26 X. Hang, J. Zhao, Y. Xue, R. Yang and H. Pang, Synergistic effect of Co/Ni bimetallic metal–organic nanostructures for enhanced electrochemical energy storage, *J. Colloid Interface Sci.*, 2022, **628**, 389–396.
27 Y. Yang, H. Dong, Y. Wang, C. He, Y. Wang and X. Zhang, Synthesis of octahedral like Cu-BTC derivatives derived from MOF calcined under different atmosphere for application in CO oxidation, *J. Solid State Chem.*, 2018, **258**, 582–587.
28 M. R. Tamtam, R. Koutavarapu, R. Wang, G. S. Choi and J. Shim, Cobalt–copper MOF: A high-performance and ecofriendly electrode material for symmetric and asymmetric supercapacitors, *Mater. Sci. Semicond. Process.*, 2025, **188**, 109220.
29 S. Huang, X. R. Shi, C. Sun, X. Zhang, M. Huang, R. Liu, H. Wang and S. Xu, Template-controlled *in situ* growing of NiCo-MOF nanosheets on Ni foam with mixed linkers for high performance asymmetric supercapacitors, *Appl. Surf. Sci.*, 2022, **572**, 151344.
30 P. Wen, P. Gong, J. Sun, J. Wang and S. Yang, Design and synthesis of Ni-MOF/CNT composites and rGO/carbon nitride composites for an asymmetric supercapacitor with high energy and power density, *J. Mater. Chem. A*, 2015, **3**, 13874–13883.
31 Y. Liang, W. Yao, J. Duan, M. Chu, S. Sun and X. Li, Nickel cobalt bimetallic metal–organic frameworks with a layer-and-channel structure for high-performance supercapacitors, *J. Energy Storage*, 2021, **33**, 102149.
32 S. Xiong, S. Jiang, J. Wang, H. Lin, M. Lin, S. Weng, S. Liu, Y. Jiao, Y. Xu and J. Chen, A high-performance hybrid supercapacitor with NiO derived NiO@ Ni-MOF composite electrodes, *Electrochim. Acta*, 2020, **340**, 135956.
33 H. Zhang, J. Wang, Y. Sun, X. Zhang, H. Yang and B. Lin, Wire spherical-shaped Co-MOF electrode materials for high-performance all-solid-state flexible asymmetric supercapacitor device, *J. Alloys Compd.*, 2021, **879**, 160423.
34 Q. Li, H. Guo, R. Xue, M. Wang, M. Xu, W. Yang, J. Zhang and W. Yang, Self-assembled Mo doped Ni-MOF nanosheets based electrode material for high performance battery-supercapacitor hybrid device, *Int. J. Hydrogen Energy*, 2020, **45**, 20820–20831.
35 S. H. Kazemi, B. Hosseinzadeh, H. Kazemi, M. A. Kiani and S. Hajati, Facile synthesis of mixed metal–organic frameworks: electrode materials for supercapacitors with excellent areal capacitance and operational stability, *ACS Appl. Mater. Interfaces*, 2018, **10**, 23063–23073.
36 J. Zeng, K. C. Devarayapalli, S. V. P. Vattikuti and J. Shim, Split-cell symmetric supercapacitor performance of bimetallic MOFs Yolk-shell hierarchical microstructure, *Mater. Lett.*, 2022, **309**, 131305.
37 S. Krishnan, A. K. Gupta, M. K. Singh, N. Guha and D. K. Rai, Nitrogen-rich Cu-MOF decorated on reduced graphene oxide nanosheets for hybrid supercapacitor applications with enhanced cycling stability, *Chem. Eng. J.*, 2022, **435**, 135042.